The Iraqi Journal For Mechanical And Material Engineering, Vol.9, No.3, 2009

Experimental and Numerical Study of Fin Heat Sinks Systems

H. A.K Shahad [*], T. A. Husain[**] , and F. H. Ali

Abstract

In this study has been compared the heat transfer performance of various commnoly fin geometries by studying the temprature and velocity distribution. Comparitive thermal tests have been carried out using aluminum heat sinks with extruded fins, staggered square pins, and staggered cylinderical pins in forced convection air flow environments. The extruded fin heat sink was designed to minimize the pressure losses across the heat sink by reducing the vortex effects to enhance the thermal performance by maintaining large exposed surfaces area available for heat transfer. Experimental and theoretical investigation were carried out.

The most electronic components operates in the range of temprature between $(40)^{o}$c and $(60)^{o}$c therfore in the experimental tests, air velocity was varied from (2) m/s to (6) m/s and the heat flux from (20) Watt to (40) Watt are used to obtain the range of temprature. The temprature of the solid structure was measured experimentally by using (15) thermocouple. They are distributed on the heat sinks uniformly.The velocity and temprature of the flow field in the test section was measured experimentally using portable anemometer.

A software packages (ANSYS 5.4) was used to carry out the theoretical study using adiabatic flow condition. This gives a good ability to calculate the velocity and pressure distributon and sketching the eddies wake behind the pins and fins in the core of the heat sink. By the aid of this software package a three-dimemsional model was built by putting horizontal orintation only. The model boundary condition can be easily varied through (ANSYS 5.4), including all ranges used in the present study. The flow was analyzed for three-dimensional steady, adiabatic, incompressible and viscous. Navir-stocks equations and continuity equation were solved. A two-equation K-ε model (turbulence model) was also solved by this program.

The straight fin experienced the lowest amount of flow by-pass over the heat sink. For this particular application, where the heat source is localized at the bottom of the heat sink base plate, the overall thermal resistance of the straight fin was lower than the other two designs mainly due to fins have large area of convection. The relative thermal resistance for cylinderical pin-fin heat sink was higher than the other two designs. This is due to the improve distribution of air flow around the circular pin.The results show that when the heat sinks have the same area of convection, the cylinderical pin-fin heat sink was the best choice while when the heat sinks have the same area of conduction the straight fin was the best choice because it give large exposed surface (large area of convection).

*** present address: Assist professor in Babylon University, Mechanical Engineering Department.**
**** present address: Assist professor in Babylon University, Material Engineering Department.**

Introduction

Electronic equipment has made its way practically through every aspect of modern life, from toys and appliances to high power computers. The reliability of electronics of a system is a major factor in the overall reliability of the system. Electronic components depend on the passage of electronic system has resulted in a dramatic increase in the amount of heat generated per unit volume, comparable in magnitude to these encountered at nuclear reactors and the surface of the sun.

Unless properly designed and controlled, high rate of heat generation results in high operating temperatures for electronic equipment, which jeopardizes its safety and reliability. The failure rate of electronic equipments increases exponentially with temperature. Also, the high thermal stress in the solder joints of electronic components mounted on circuit boards resulting from temperature variation are major causes of failure. Therefore, thermal controls have become increasingly important in the design and operation of electronic equipments[1].

Flow through heat sinks refers to heat sinks wherein the flow inters the heat sinks from one end and travels more or less in a straight line to exit from the other end. One of the simplest, and most cost-effective heat sink designs used is the linearly extruded aluminum heat sink. Aluminum has many characteristics that make it an excellent heat sink material. It is easily in fine detail with inexpensive tooling. These heat sinks can be extruded to a maximum fin density ratio (the height to width spacing between fins) of approximately (5) to (1). This limit is a result of manufacturing costs and tolerance control, as described by Kiley and Soule (1990)[2]. Such heat sinks are commonly used for many application, but are limited to relatively low-power dissipation due to the limitation of total surface area per volume.

Higher aspect ratios of up to (25) or more can be attained by using epoxy-bonded fin heat sinks. These heat sinks consist of an extruded or machined base, which is flat on the module-facing side and grooved. The fins are then epoxies into the grooves. The epoxy interface does, however, add a thermal resistance to the system. This difficulty can be overcome by brazing or soldering the fins to the base, resulting in reduced overall resistance at a higher coast, Kiley and Soule (1990)[2] and Soule (1993)[3]. Both aluminum and copper can be used to construct this type of heat sink, depending on the system requirements and allowable overall weight.

Tuckerman and Pease (1981)[4] had designed a silicon micro heat sink based upon this principle and were able to dissipate very high heat flux levels, (790) W/cm^2 with associated water temperature of (70) ^{0}C based upon the same principle (micro channels).

Goldberg (1984)[5] had proposed a laminar flow copper heat sink for air cooling capable of delivering heat flux in excess of (25) W/cm^2 at the chip level with an associated air temperature of (60) ^{0}C.

Pin-fin heat sinks are also commonly used and have the add advantage of not requiring specific positioning relative to flow direction. Pin-fin heat sinks can be manufactured either by starting with a linearly extruded parallel plate heat sink and then cutting the plates to form the pins, or by building them using more costly specialized techniques such as epoxy bonding, brazing and soldering. Round pins or other cross-section shapes can also be manufactured using casting[6].

Minakami *et al*. (1992)[7] had reported a flow through cooled heat sink using miniature pins, the side length of the copper pins had only (0.19)mm manufactured by etching. It was found that the pin spacing in the flow direction, for optimal thermal performance had about (4.5) pin diameters. The heat transfer increased monotonically as the transverse fin pitch decreased, with an associated penalty in pressure drop increase.

Shaukatullah *et al*. (1996)[8] had reported an experimental optimization study of pin-fin array in cross flow with low velocities. Pin-fin array from (4x4) to (8x8), height from(5 to 25)mm and width from (1.5 to 2.5)mm. Results showed that a different optimal heat sink design existed from every flow velocity.

In the present work, three types of heat sinks which are commonly used to cool electronic components were studied, Square pin-fin, Cylindrical pin-fin and longitudinal fins (extruded fin). All the heat sinks are made of aluminum with thermal conductivity (157) W/m.^{0}C and the base dimension of the heat sink are (110) mm Length, (100) mm Width, and (15) mm Thickness. The height of the fins are kept at (68) mm. The three types of heat sink have the same area of conduction. Fig. (1) describes three types of heat sink configurations.

The objective of the present work is to study temperature and velocity distribution of three types of heat sinks at different inlet velocity and heat flux by using experimental and numerical techniques. The inlet velocity of air varies from (2,3,4 to 6) m/s and heat flux from (20,30 to 40) Watt.

An experimental study has been carried out in the heat transfer Lab in Babylon University by using Free and Force Convection Heat Transfer Units which are made by P.A.Hilton LTD (England). Changes in some of its parts are made to suit our study.

A numerical study has been obtained by using Computational Fluid Dynamic techniques. A three-dimensional solid model was constructed using Ansys package. Its dimension are equal to the actual dimensions. In the theoretical calculation we can calculate velocity values in three dimensions, resultant velocity, velocity vector, are predicted.

Computational Analysis

The governing equations solved for the flow field are the continuity, momentum and energy equations in three dimensions, and these are;

$$\frac{\partial \rho}{\partial t}+\frac{\partial(\rho v_x)}{\partial x}+\frac{\partial(\rho v_y)}{\partial y}+\frac{\partial(\rho v_z)}{\partial z}=0 \qquad (1)$$

$$\rho(\frac{\partial u}{\partial t}+q\nabla u)=\rho Xx-\frac{\partial p}{\partial x}+\frac{\partial}{\partial x}\left\{\mu\left[2\frac{\partial u}{\partial x}-\frac{2}{3}(divq)\right]\right\}+\frac{\partial}{\partial y}\left[\mu\left(\frac{\partial u}{\partial y}+\frac{\partial v}{\partial x}\right)\right]+\frac{\partial}{\partial z}\left[\mu\left(\frac{\partial w}{\partial x}+\frac{\partial u}{\partial z}\right)\right] \qquad (2)$$

$\rho\left(\frac{\partial v}{\partial t}+q\nabla V\right)=\rho Xy-\frac{\partial p}{\partial y}+\frac{\partial}{\partial y}\left\{\mu\left[2\frac{\partial v}{\partial y}-\frac{2}{3}(divq)\right]\right\}+\frac{\partial}{\partial z}\left[\mu\left(\frac{\partial v}{\partial z}+\frac{\partial w}{\partial y}\right)\right]+\frac{\partial}{\partial x}\left[\mu\left(\frac{\partial u}{\partial y}+\frac{\partial v}{\partial x}\right)\right]$	**(3)**

$\rho\left(\frac{\partial w}{\partial t}+q\nabla w\right)=\rho Xz-\frac{\partial p}{\partial z}+\frac{\partial}{\partial z}\left\{\mu\left[2\frac{\partial w}{\partial z}-\frac{2}{3}(divq)\right]\right\}+\frac{\partial}{\partial x}\left[\mu\left(\frac{\partial w}{\partial x}+\frac{\partial u}{\partial z}\right)\right]+\frac{\partial}{\partial y}\left[\mu\left(\frac{\partial v}{\partial z}+\frac{\partial w}{\partial y}\right)\right]$	**(4)**

The equation above are the Navir-Stockes equation and energy equation[9]. Some terms must be eliminated when solving the problem. For the steady state analysis the time dependent term must be eliminated. The density enters as a constant value. Therefore, the final form of the continuity and momentum equations is as follow;

$\frac{\partial v_x}{\partial x}+\frac{\partial v_y}{\partial y}+\frac{\partial v_z}{\partial z}=0$	**(5)**

$\rho(u\frac{\partial u}{\partial x}+v\frac{\partial u}{\partial y}+w\frac{\partial u}{\partial z})=-\frac{\partial p}{\partial x}+\mu_e\left(\frac{\partial^2 u}{\partial x^2}+\frac{\partial^2 u}{\partial y^2}+\frac{\partial^2 u}{\partial z^2}\right)$	**(6)**

$\rho(u\frac{\partial v}{\partial x}+v\frac{\partial v}{\partial y}+w\frac{\partial v}{\partial z})=-\frac{\partial p}{\partial x}+\mu_e\left(\frac{\partial^2 v}{\partial x^2}+\frac{\partial^2 v}{\partial y^2}+\frac{\partial^2 v}{\partial z^2}\right)$	**(7)**

$\rho(u\frac{\partial w}{\partial x}+v\frac{\partial w}{\partial y}+w\frac{\partial w}{\partial z})=-\frac{\partial p}{\partial x}+\mu_e\left(\frac{\partial^2 w}{\partial x^2}+\frac{\partial^2 w}{\partial y^2}+\frac{\partial^2 w}{\partial z^2}\right)$	**(8)**

$u\frac{\partial T}{\partial x}+v\frac{\partial T}{\partial y}+w\frac{\partial T}{\partial z}=-\frac{\partial p}{\partial x}+\alpha\left(\frac{\partial^2 T}{\partial x^2}+\frac{\partial^2 T}{\partial y^2}+\frac{\partial^2 T}{\partial z^2}\right)$	**(9)**

For the turbulent case the effective viscosity ($\mu_e=\mu+\mu_t$).

Where; μ=Laminar viscosity, μ_t=Turbulent viscosity, α=Thermal diffusivity.

The governing equation for the solid field (heat sink) is only the right side of the energy equation.

$\frac{\partial^2 T}{\partial x^2}+\frac{\partial^2 T}{\partial y^2}+\frac{\partial^2 T}{\partial z^2}=0$	**(*10*)**

An element based on Finite Element method was used for simulating conduction and convection. This is coupled with an unstructured element based finite element Computational Fluid Dynamics (CFD) code which solves the complete Navir-Stockes equations. A unique thermal coupling method allows ANSYS software to simulate convective and conduction heat paths between disjoint element meshes on arbitrary geometry. This coupled is very complex in the ANSYS software package and does not have enough information, therefore, the solution in the present study solves the continuity and momentum equations (adiabatic flow) for three dimensional.

The theoretical results presented in this paper are obtained by ANSYS program. This software package solves the fluid flow problem by solving momentum and continuity equation. The two equations K-ε model (turbulence model) is used to present the turbulence in the flow. By using the finite element technique, this program analyzes the flow field through the heat sink models. There are many types of meshing controls where the boundary conditions can be changed to overcome all the actual boundary conditions.

The partial differential equations solved by FLOTRAN in two equation models, the Turbulent Kinetic Energy equation is

$\frac{\partial \rho k}{\partial t}+\frac{\partial(\rho v_x k)}{\partial x}+\frac{\partial(\rho v_y k)}{\partial y}+\frac{\partial(\rho v_z k)}{\partial z}=\frac{\partial}{\partial x}\left(\frac{\mu_t}{\sigma_k}\frac{\partial k}{\partial x}\right)+\frac{\partial}{\partial y}\left(\frac{\mu_t}{\sigma_k}\frac{\partial k}{\partial y}\right)+$ $\frac{\partial}{\partial z}\left(\frac{\mu_t}{\sigma_k}\frac{\partial k}{\partial z}\right)+\mu_t\phi-\rho\varepsilon+\frac{C_4\beta\mu_t}{\sigma_t}\left(g_x\frac{\partial T}{\partial x}+g_y\frac{\partial T}{\partial y}+g_z\frac{\partial T}{\partial z}\right)$	**(*11*)**

and the Dissipation Rate equation is

$\frac{\partial \rho\varepsilon}{\partial t}+\frac{\partial(\rho v_x \varepsilon)}{\partial x}+\frac{\partial(\rho v_y \varepsilon)}{\partial y}+\frac{\partial(\rho v_z \varepsilon)}{\partial z}=\frac{\partial}{\partial x}\left(\frac{\mu_t}{\sigma_\varepsilon}\frac{\partial \varepsilon}{\partial x}\right)+\frac{\partial}{\partial y}\left(\frac{\mu_t}{\sigma_\varepsilon}\frac{\partial \varepsilon}{\partial y}\right)+$ $\frac{\partial}{\partial z}\left(\frac{\mu_t}{\sigma_\varepsilon}\frac{\partial \varepsilon}{\partial z}\right)+C_{1\varepsilon}\mu_t\frac{\varepsilon}{k}\phi-C_2\rho\frac{\varepsilon^2}{k}+$ $\frac{C_\mu(1-C_3)\beta\rho k}{\sigma_t}\left(g_x\frac{\partial T}{\partial x}+g_y\frac{\partial T}{\partial y}+g_z\frac{\partial T}{\partial z}\right)$	**(*12*)**

$$\mu_t = \rho C_\mu \frac{k^2}{\varepsilon}$$	**(*13*)**

The final term in each equation are terms used to model the effect of buoyancy are described by Viollet[10]. Default values for the various constants in the standard model are provided by Lauder and Spalding[9] and are given in Standard Model coefficients.

$C_1, C_{1\varepsilon}$	C_2	C_μ	σ_k	σ_ε	σ_t	C_3	C_4
1.44	1.92	0.09	1.0	1.3	1.0	1.0	0.0

Table (1) Standard Model Coefficients.

Measurement

The main aim of the research is to specifying a better performance and heat dissipation of three types of heat sinks by studying the velocity and temperature distribution and locating the heat transfer coefficient for several air speed and heat flux. All these parameter required building up the main experimental rig.

The velocity had been measured at the entrance of the duct to select a suitable velocity value which was (2), (3), (4), and (6) m/s. Also measured velocity and temperature in selecting position as shown in Figs (2), (3), and (4) marked by (A_{1-1}, B_{1-1}, C_{1-1}, D_{1-1}…etc) which was given its coordinates (x, y, z) in the test section (heat sink) which gave us body contour for the velocity and temperature distribution in the test section. Fig(2) represent the position for measuring the air velocity and temperature for the cylindrical pin-fin heat sink, Fig(3) represent the position of measuring the air velocity and temperature for the square pin-fin heat sink. Fig (4) represent the positions of measuring the air velocity and temperature for the longitudinal fin heat sink.

Fig. (5) shows the experimental apparatus consisting of centrifugal fan. Test section control system for power supply heat flux and thermocouples for temperature measurement in flow field and on the heat sinks, and portable anemometer to measure the velocity at a selector positions are shown in Figs. (2), (3), (4). Moreover a new positions for measured velocity and temperature on the heat sink have been chosen to give more accurate results.

Results and Discussion

Fig. (6) shows the experimental effect of increasing velocity on the thermal resistance for each heat sink and for different heat loads. The results show that the thermal resistance of square pin-fin is higher than the thermal resistance for cylindrical pin-fin. Thermal resistance for cylinder pin-fin heat sink is higher than for longitudinal fin heat sink. Same behavior is obtained for all heat loads. This is due to the fact that velocity distribution was more uniform through the longitudinal fin heat sink which increases the heat transfer coefficient and decreases the base temperature and decreases the thermal resistance. Also, the areas of convection for longitudinal fin heat sink is higher than the area of convection for cylindrical and square pin-fin. The difference between curves reaches a minimum value at maximum studied velocity due to higher mass of air across the heat sinks.

Fig. (7) shows the experimental relative thermal resistance which was obtained by dividing the thermal resistance to the surface area of convection for each type of heat sink compared with the results obtained by Arnold [11]. Fig. (7) illustrates a good agreement obtained in calculating the steady state by experimental results. The results show that the relative thermal resistance of cylindrical pin-fin is higher than the relative thermal resistance for square pin-fin, and the relative thermal resistance for square pin-fin is higher than that for longitudinal fin. This is due to the surface area of convection heat transfer where the longitudinal fin heat sink has maximum surface area of convection which is equal to (1149.36) cm^2. The surface area of convection for square pin-fin is equal to (529.21) cm^2, and for the cylinder pin-fin it is equal to (474.822) cm^2 while the three types of heat sinks have the same area of conduction which was equal to (3.25) cm^2. The longitudinal fin maintains large expose surface area available for heat transfer.

Fig. (8) shows the minimum local heat transfer coefficient experimentally where the heat flux (20) Watt and velocity (2) m/s. Fig. (9) shows the maximum local heat transfer coefficient experimentally where conditions are (40) Watt heat flux and (6) m/s velocity. The local heat transfer coefficient is increased with the direction of flow in longitudinal heat sink while the local heat transfer coefficient is decreased with the flow for both cylindrical and square pin-fin. This is as a result of thermal boundary layer development from the entrance of the heat sink towards the exit. This boundary layer is developed in the case of longitudinal heat sink because the flow has no restriction on its flow. The heat sink has no clearance above it and no large space in the two sides of the heat sink. Also with increasing distance from the leading edge the effect of heat transfer penetrates further into the free stream and the thermal boundary layers grow. Therefore the thermal boundary layer is more effective in longitudinal fin heat sink while the thermal boundary layer is less effective in pin-fin because of the small area of attach.

Fig. (10) shows the effect of air flow velocity for experimental and theoretical results, where significant flow By-Pass is seen with square pin-fin heat sink. This is of no surprise since the cross-section of this heat sink represents more of an obstruction for air flow. Also, Cylinder pin-fin induced more flow By-Pass than the straight fin, suggesting increase turbulence and pressure drop for ail heat sinks, The largest mount of By-Pass is at maximum air velocity. The theoretical results was lower than experimental results this is for adiabatic flow were studied for theoretical results. In the experimental results we can read the velocity of air in the x-direction ($v_x=u$) at given local coordinates (x , y) by using portable anemometer at three domains of z-direction (z=0.0226 m) from the base which marked (a), (z=0.0453 m) from the base which marked (b) and (z=0.068 m) from the base which marked (c). This results enable us to give a good picture of velocity distribution. This section presents the velocity profiles only for inlet velocity (2) m/s and thermal power (20) Watt.

Fig. (11) shows the calculated velocity distribution for cylinder pin-fin heat sink at three domains with entrance velocity which is equal to (2) m/s. Fig. (12) shows the velocity distribution for square pin-fin heat sink at three domains with entrance velocity which is equal to (2) m/s. Fig. (13) shows the velocity distribution for longitudinal fin heat sink at three domains with entrance velocity which is equal to (2) m/s. From these Figs. we can show the difference between velocity distribution for cylinder and square pin-fin heat sink, which is due to the shape of pin-fin. The air flow around is more improved distribution from the square pin-fin. Square pin-fin has a sharp angle in four corners which promote dead zone behind each pin. The values of velocity for square pin-fin is smaller than those for cylinder pin-fin. For square pin-fin heat sink of the second domain has large values of velocity because it was in the middle distance of the channel. In longitudinal fin heat sink the air flow enters the grooves between fins. This process is like the flow parallel plate channel. When velocity enters the grooves the velocity boundary layer starts to grow on the surface of fin on the other surface the velocity boundary layer starts to grow also. At the distance from the leading edge the two boundary layers were attached and the velocity at this point reaches its maximum. These grooves represent a good straight path to the air flow to move on it. The value of velocity increases toward the flow in this type of heat sink. For this reason the velocity distribution for longitudinal fin heat sink is more uniform than that in cylindrical and square pin-fin heat sink. There are also no large different between the inlet and outlet heat sink velocity. For longitudinal fin heat sink the maximum value of velocity can be shown in the second domain because this domain in the middle distance of the channel.

Fig. (14) shows the experimental Isothermal contour temperature field for cylindrical pin-fin heat sink at three domains. Fig. (15) shows the experimental Isothermal contour temperature field for square pin-fin heat sink at three domains. Fig. (16) shows the experimental Isothermal contour temperature field for longitudinal fin heat sink at three domains. It is evident that the lowest temperature in the air stream is at the beginning of the heat sink for this type of heat sink; this is on the left side. The temperature raises as the air passes through the heat exchanging structure. Therefore the highest temperatures are noted at the exit; this is on the right side. The lowest temperature in the domain is in the third domain which is the upper domain and the highest on the bottom (first domain) close to the base-plate. Because the heat flux is a vector perpendicular to the isotherms, a qualitative picture of heat flow can be extracted from the calculated temperature fields. It can be seen in this fig. that most of the heat is transfered from the solid to fluid in the first half of the test section. The highest heat fluxes appear in the middle left corner, where the temperature gradients are the highest. The second half of the heat sink does not participate in the heat transfer process. From Figs. (14, 15, 16), it is revealed that in the nearest to the base-plate the temperature field is not fully developed. This means that the air which enters the test section is quickly heated due to the nearest to the base-plate and leaves the heat sink at the temperature nearest to the base temperature. With increasing distance from the base-plate temperature field becomes more developed. This phenomenon also occurs with inlet velocity increasing where at low velocity the temperature field is not fully developed. This means that air, which enters the test section, is quickly heated due to its low velocity and leaves the heat sink at the temperature of the solid-phase, unable to receive additional heat from the source. With increasing inlet velocity, the state of thermal saturation diminishes. This means that, with increasing inlet velocity, the air flow leaves the heat sink at lower exit temperature. Such coolant flow is thermally unsaturated, still capable of heat removal. Nevertheless, as the average temperature decreases, the role of heat conducting base-plate increases. This causes further reduction in the air and structure temperatures at the simulation domain exit.

Fig. (17) shows the theoretical velocity distribution for cylinder pin-fin heat sink at the three domains with inlet velocity which is equal to (2) m/s. Fig. (18) shows the theoretical velocity distribution for square pin-fin heat sink at three domains with inlet velocity (2) m/s. Fig. (19) shows the velocity distribution for longitudinal fin heat sink at three domains with inlet velocity (2) m/s. The results of theoretical work gives us a clearer picture than that obtained from experimental results. This is due to the fact that the solution of the governing equation occurs in each node in the test section. The test section contains a lot of nodes and elements, therefore, the solution is more accurate. Fig. (19) show that the maximum velocity occurs on each side of heat sink which can namely Side-bypass. Therefore ,the Side-by pass of air should be minimized to improve the heat dissipation.

Conclusions

A fair comparison of various heat sink geometries has been attempted. These were simplified by assuming adiabatic three-dimensional flow and isothermal heat transfer surfaces. The result show that longitudinal fin heat sink geometry perform better that cylindrical and square pin-fin heat sink geometries when it has the same area of conduction because the longitudinal fin gives high expose area (large area of convection).

The cylindrical pin-fin heat sink have highest relative thermal resistance than that longitudinal and square pin-fin, this means that cylindrical pin-fin have higher performance for the same area of convection.

The manufacturing process for longitudinal fin heat sink is easier and lower in cost than the manufacturing of staggered cylinder and square pin-fin. This is due to the fact that the manufacturing process occurs on the one part of material by making grooves on it with dimensions that we need. But for staggered cylinder and square pin-fin the manufacturing process occurs on higher than one part of materials. The base of heat sink is manufactured alone and each pin is also manufactured alone. This increases the cost and time of processing also it increases the thermal resistance.

The shape and arrangement of longitudinal fin heat sink gives more surface area than cylinder and square pin-fin heat sink for the same base plate dimension.

References

[1] Yunus, A.C., **"Heat Transfer: A practical Approach"** McGraw-Hill, New York, (1997).

[2] Kily, R.F, and Soul, C.A**,"Engneering Heat Sink",** Powertechnics Magazine, July, (1990).

[3] Soul, C.A., **"Air and Liquid Cooled Techniques for High Power Density Components",** Power Conservation and Intelligent Motion, Vol.19,No.11, (1993).

[4] Tuckerman, D.B., and Pease, R.F.W., **"High Performance Heat Sinking for VLSI",** IEEE Electron Dev. Letters, Vol. EDL-2,No.5, pp.126-129,(1981).

[5] Goldberg, N., **"Narrow Channel Forced Air Heat Sink",** IEEE Transactions as on Components, Hybrids and Manufacturing Technology, Vol. CHMT-7,No.1,Mar. (1984).

[6] Azar, K., and Mandrone, C,A., **"Effect of Pin-Fin Density of the Thermal Performance of un Shrouded Pin-Fin Heat Sink",** Asme J. Electronic Packaging Vol. 116, pp.306-309, (1994).

[7] Minakami, K., Mochizuki, S., Murata, A., and Yagi, Y., **"High Performance Air-Cooling for LSIs Utilizing a Pin-Fin Heat Sink",** Paper No.92-WA/EEP-5, Asme Winter Annual Meeting, Anaheim, CA.(1992).
[8] Shaukatullah, H., Storr, W.R., Hanse, B.J., and Gaynes, M.A., **"Design and Optimization of Pin-Fin Heat Sinks for Low Velocity Application",** 12th IEEE Semi-Therm Symposium Proceedings, pp.151-163. (1996).
[9] Launder, B.E., Spalding, D.B., **"The Numerical Computation of Turbulent Flows",** Computer Method In Applied Mechanics and Engineering, Vol. 3,pp269-289, (1974).
[10] Viollet, P. L., **"The Modeling of Turbulent Recalculating Flow for the Purpose of Reactor Thermal-Hydraulic Analysis"**, Nuclear Engineering and Design, Vol. 99, pp 145-187. (1987).
[11] Arnold, F.J., Richard, R., and Jeffery, L., **"Recent Advances in Thermal/Flow Simulation: Integrating Thermal Analysis in to the Mechanical Design Process",** Eleventh IEEE SEMI-THERM™, February. (1995).

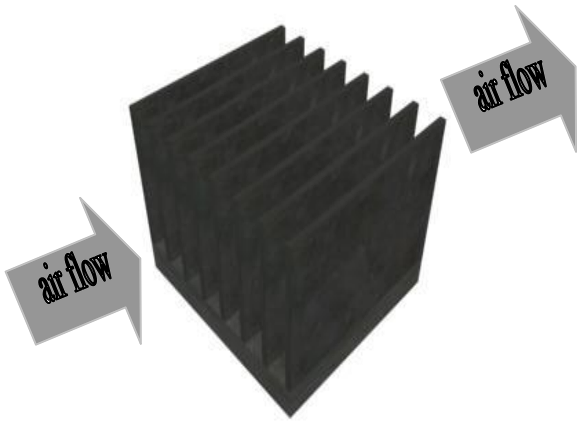

Longitudinal fin heat sink.

Fig. (1) Description of geometries of the present study.

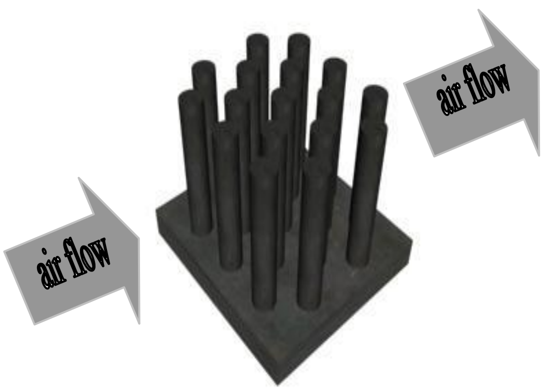

Cylindrical pin-fin heat sink.

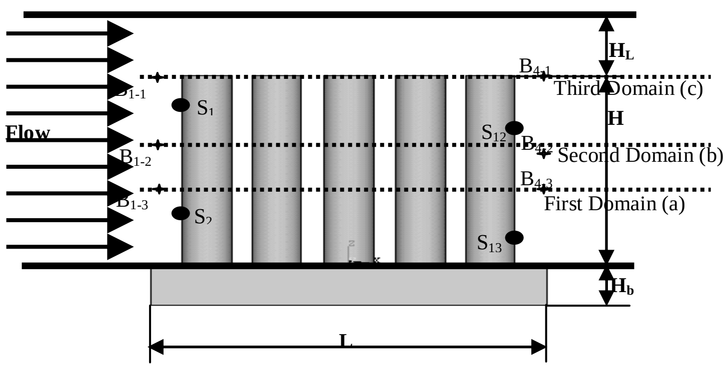

Fig. (2) Positions of temperature and velocity measurement for cylindrical pin-fin.

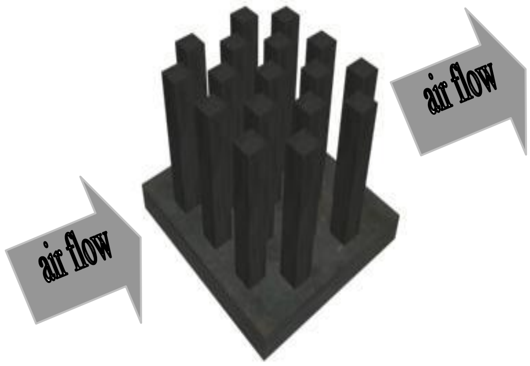

Square pin-fin heat sink.

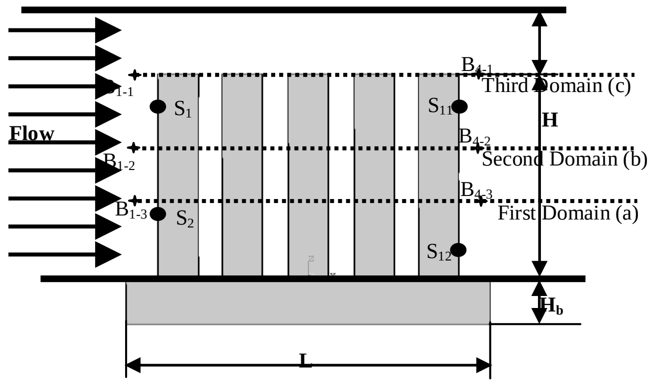

Fig. (3) Positions of temperature and velocity measurement for square pin-Fin.

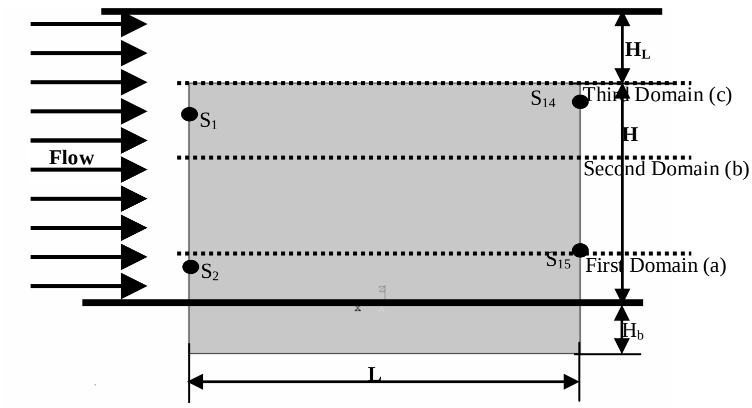

Fig. (4) Positions of temperature and velocity measurement for longitudinal fin.

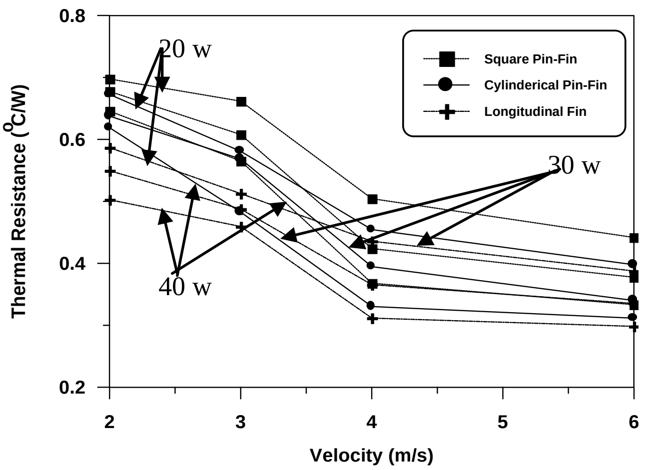

Fig.(6) Thermal Resistance vs. Air Velocity for different heat fluxes (Experimental).

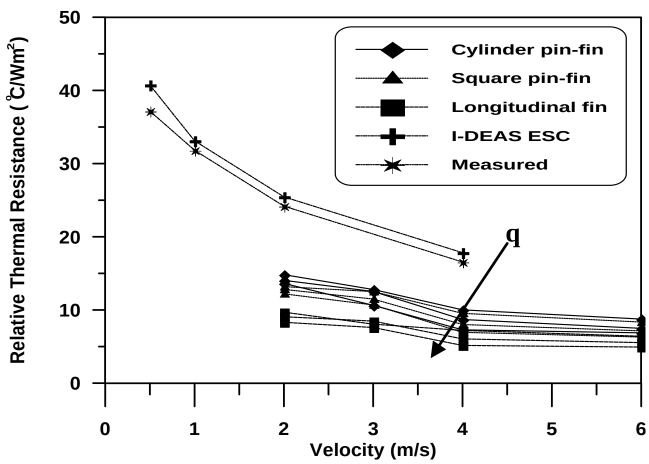

Fig.(7) Comparison of Relative Thermal Resistance vs. Air Velocity

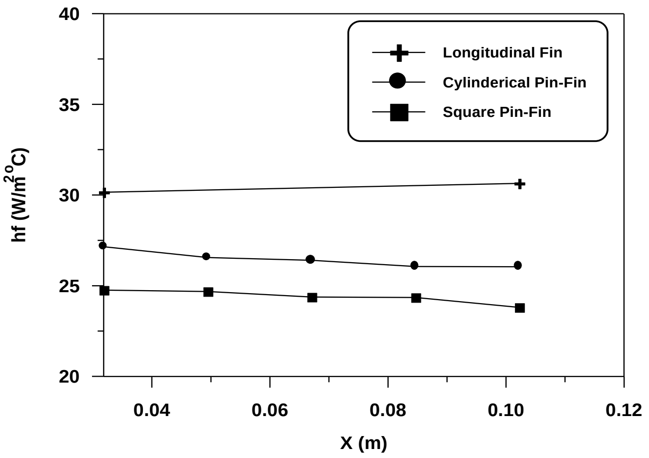

Fig.(8) Local Heat Transfer Coefficient along Flow Direction for Velocity (2) m/s and Heat Flux (20) Watt (Experimental).

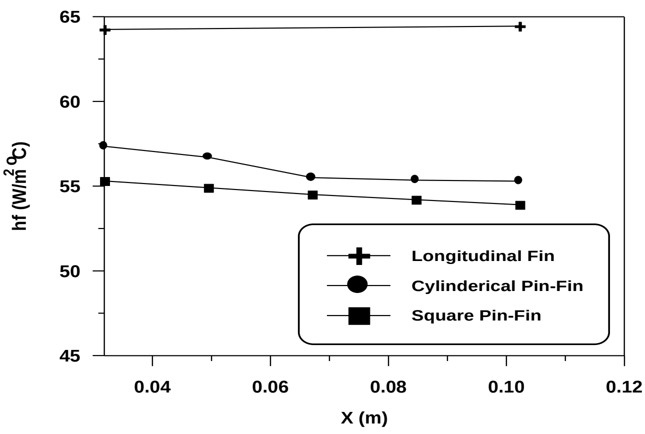

Fig.(9) Local Heat Transfer Coefficient along Flow Direction for Velocity (6) m/s and Heat Flux (40) Watt (Experimental).

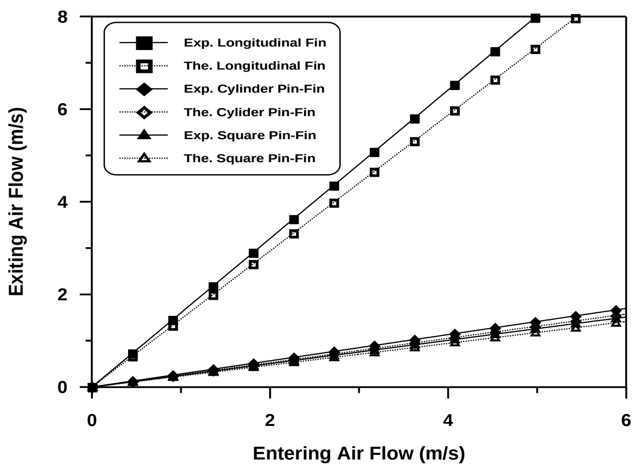

Fig. (10) Dynamic Correlation of Effective Air Flow through a Heat Sinks (Experimental).

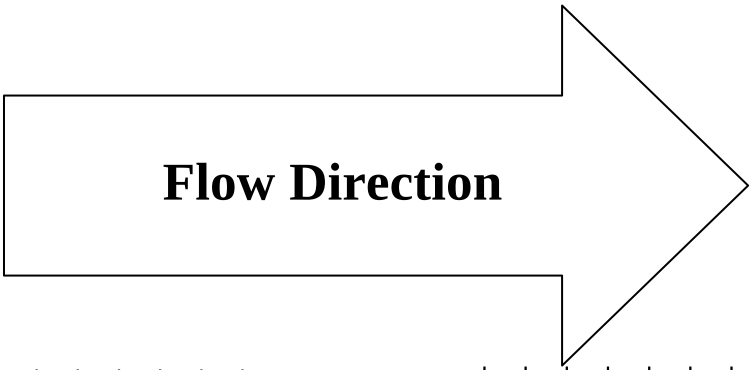

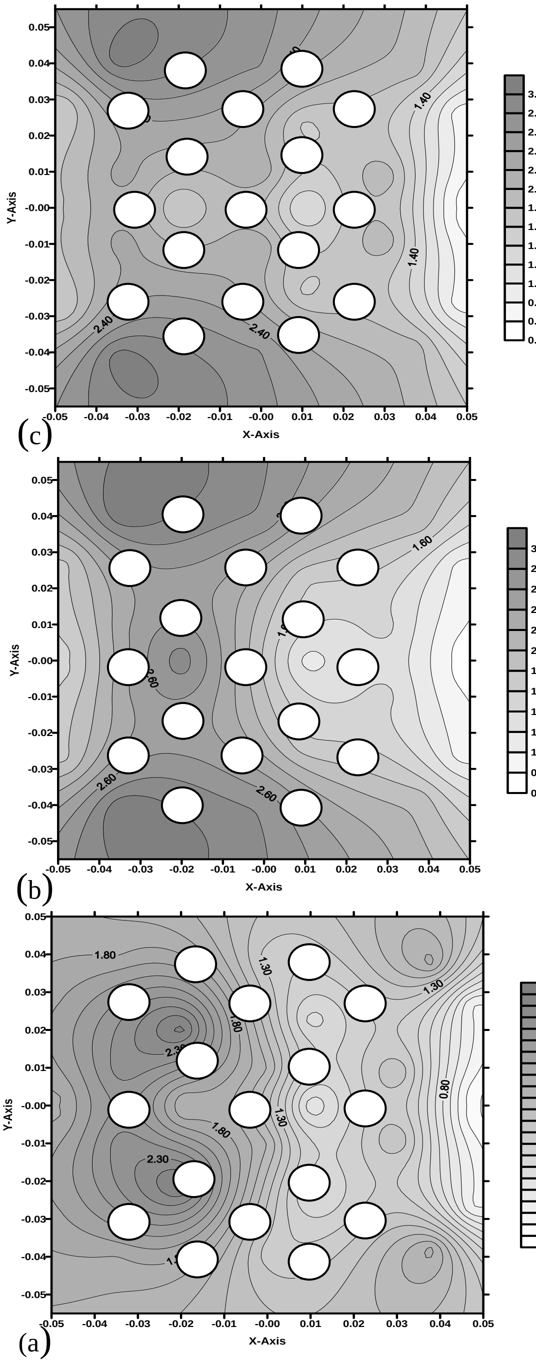

Fig. (11) Velocity Contour Map for Cylinder Pin-Fins in The First Domain (a), Second Domain (b), and Third Domain (c) (Experimental).

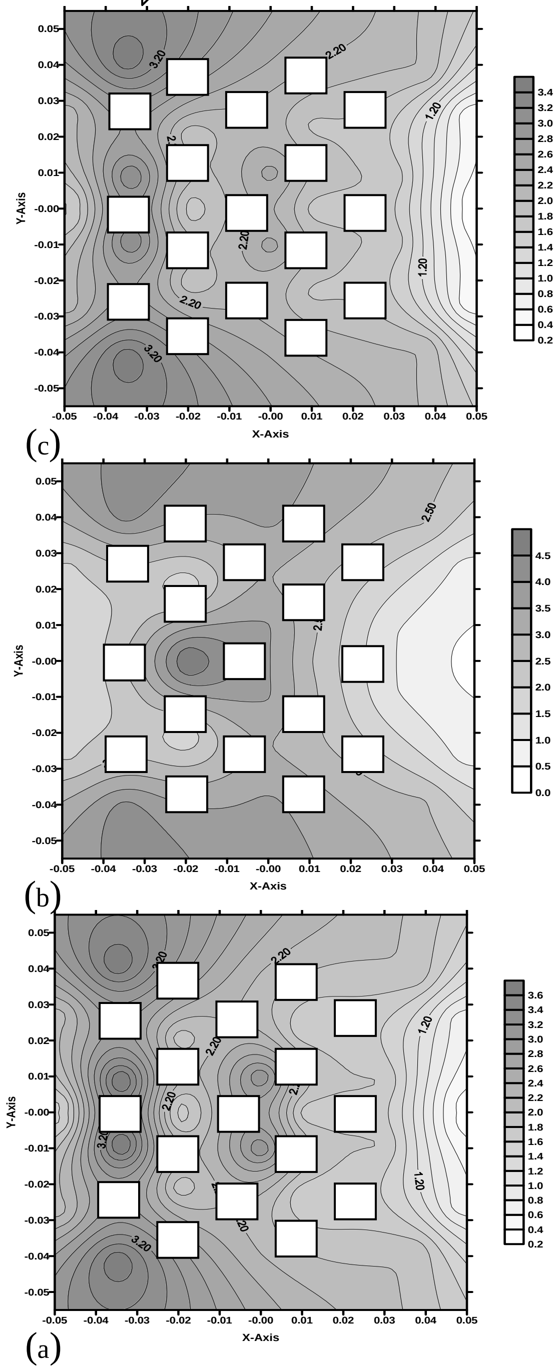

Fig. (12) Velocity Contour Map for Square Pin-Fins in The First Domain (a), Second Domain (b), and Third Domain (c) (Experimental).

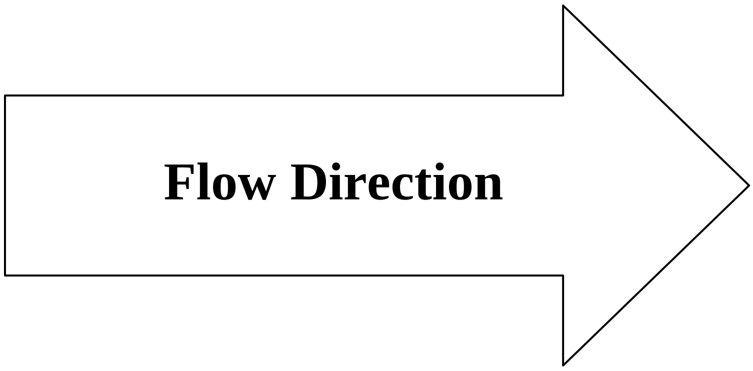

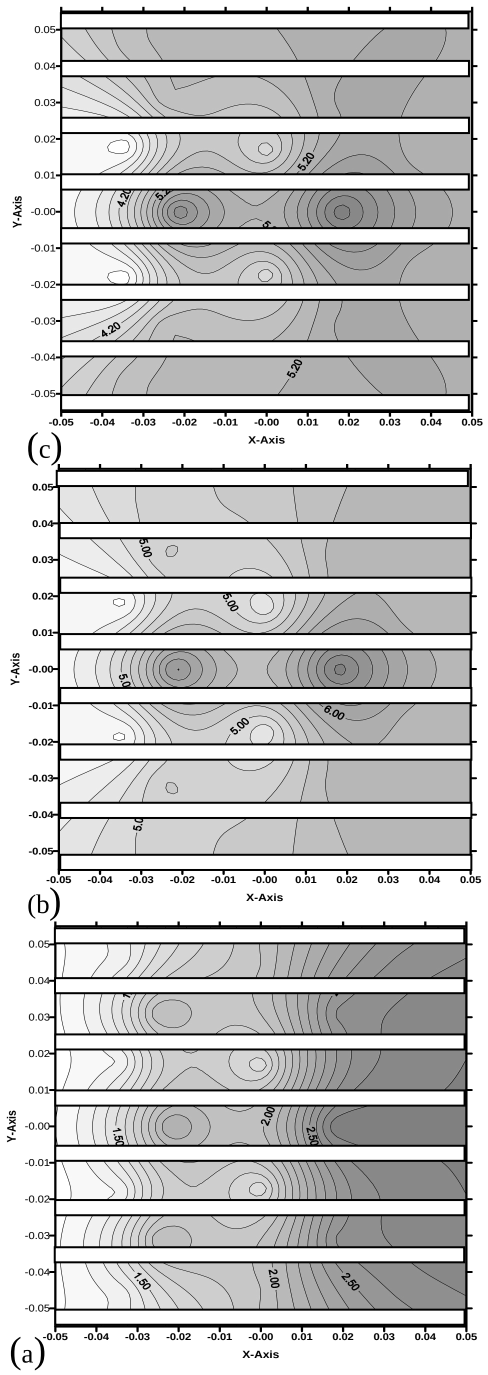

Fig. (13) Velocity Contour Map for Longitudinal Fins in The First Domain (a), Second Domain (b), and Third Domain (c) (Experimental).

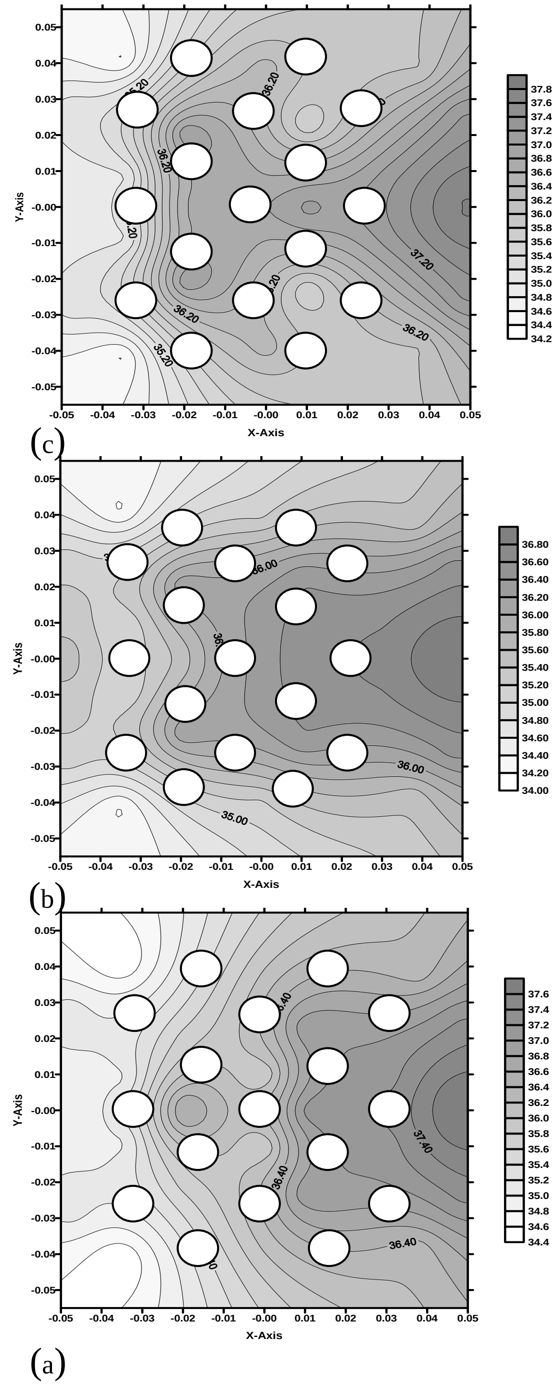

Fig. (14) Isothermal Contour Map for Cylindrical Pin-Fin in The First Domain (a), Second Domain (b), and Third Domain (c) (Experimental).

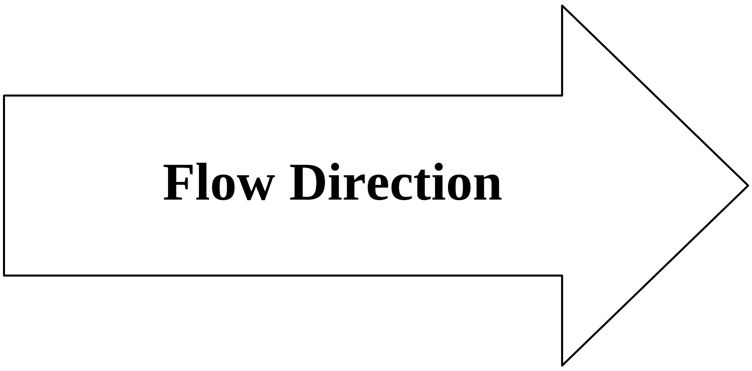

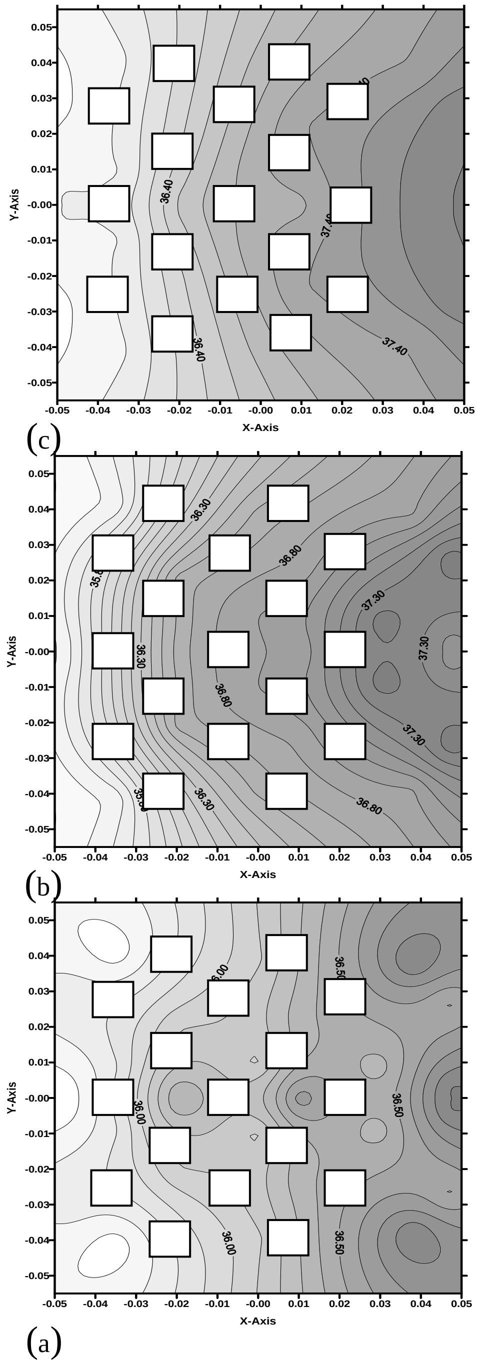

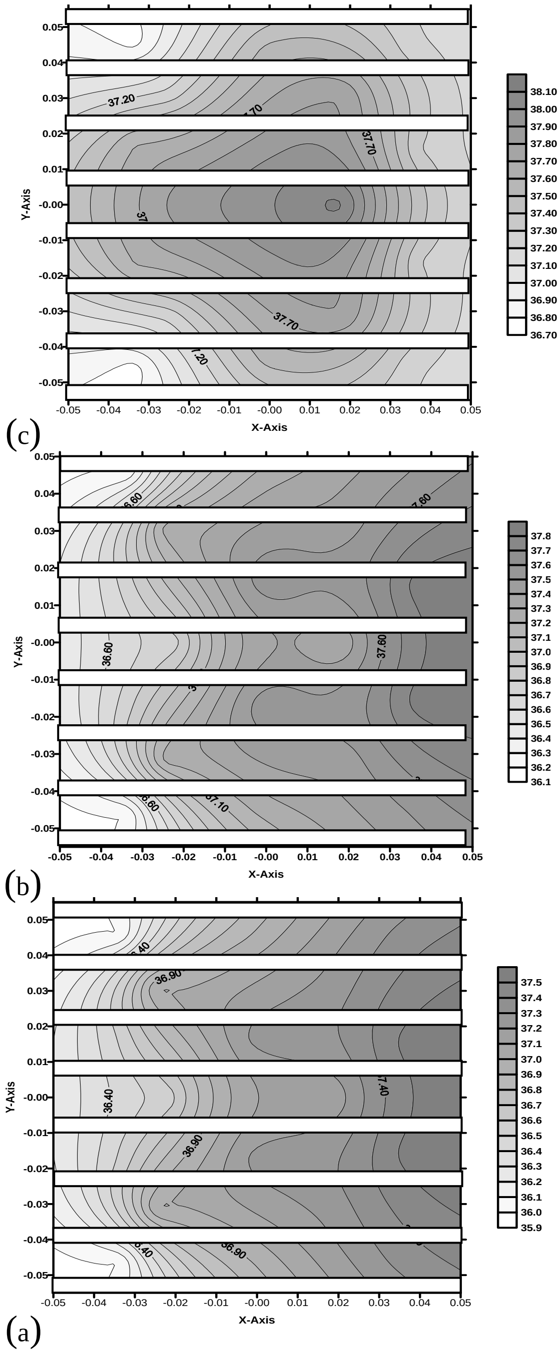

Fig. (15) Isothermal Contour Map for Square Pin-Fin in The First Domain (a), Second Domain (b), and Third Domain (c) (Experimental).

Fig. (16) Isothermal Contour Map for Longitudinal Fin in The First Domain (a), Second Domain (b), and Third Domain (c) (Experimental).

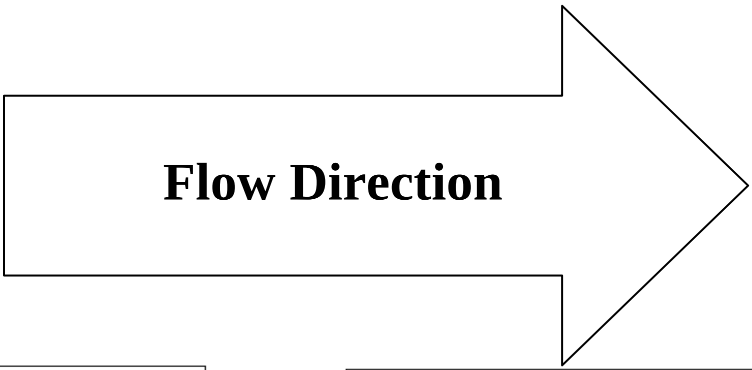

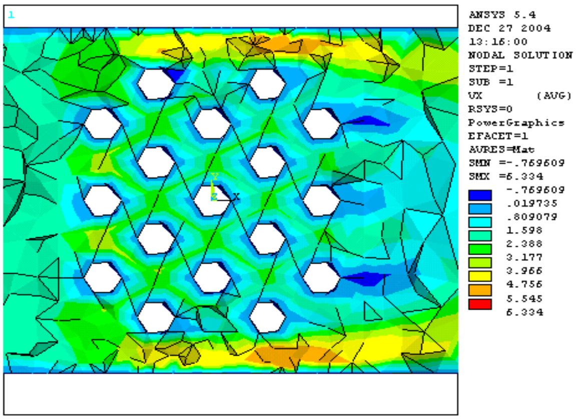

(c)

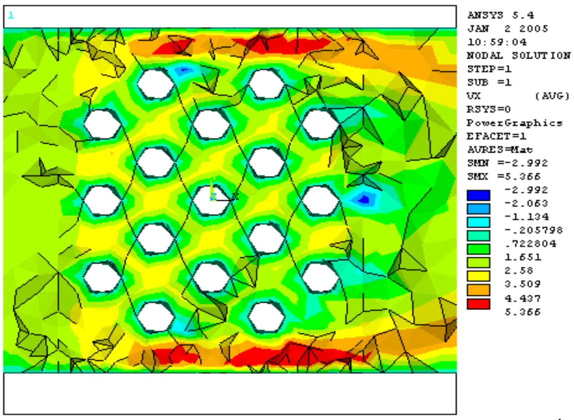

(b)

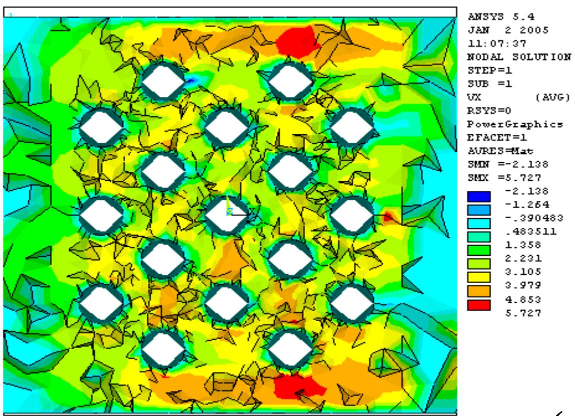

(a)

Fig. (17) Velocity Contour Map for Cylindrical Pin-Fin in the First Domain (a), Second Domain (b), Third Domain (c) (Numerical).

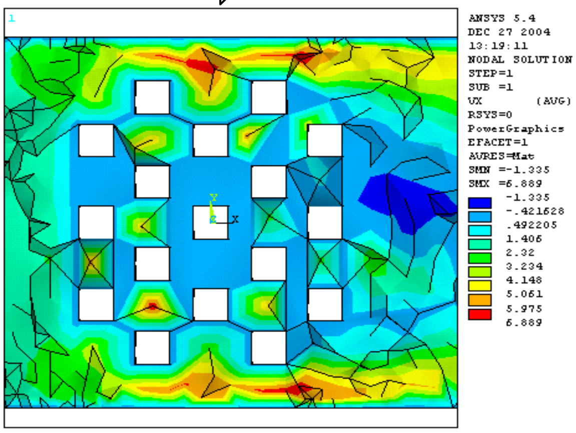

(c)

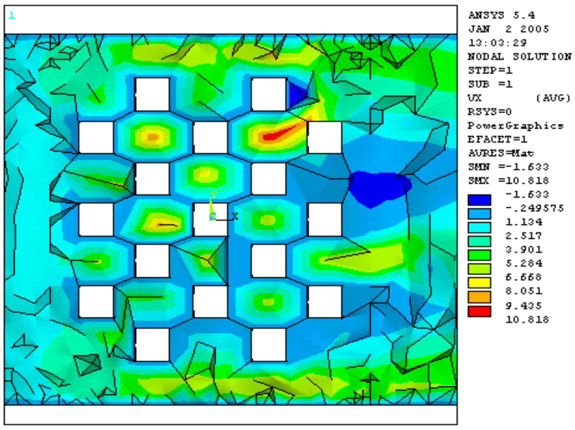

(b)

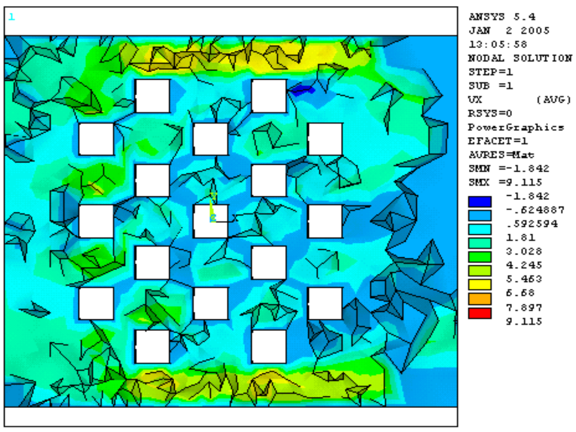

(a)

Fig. (18) Velocity Contour Map for Square Pin-Fin in the First Domain (a), Second Domain (b), Third Domain (c) (Numerical).

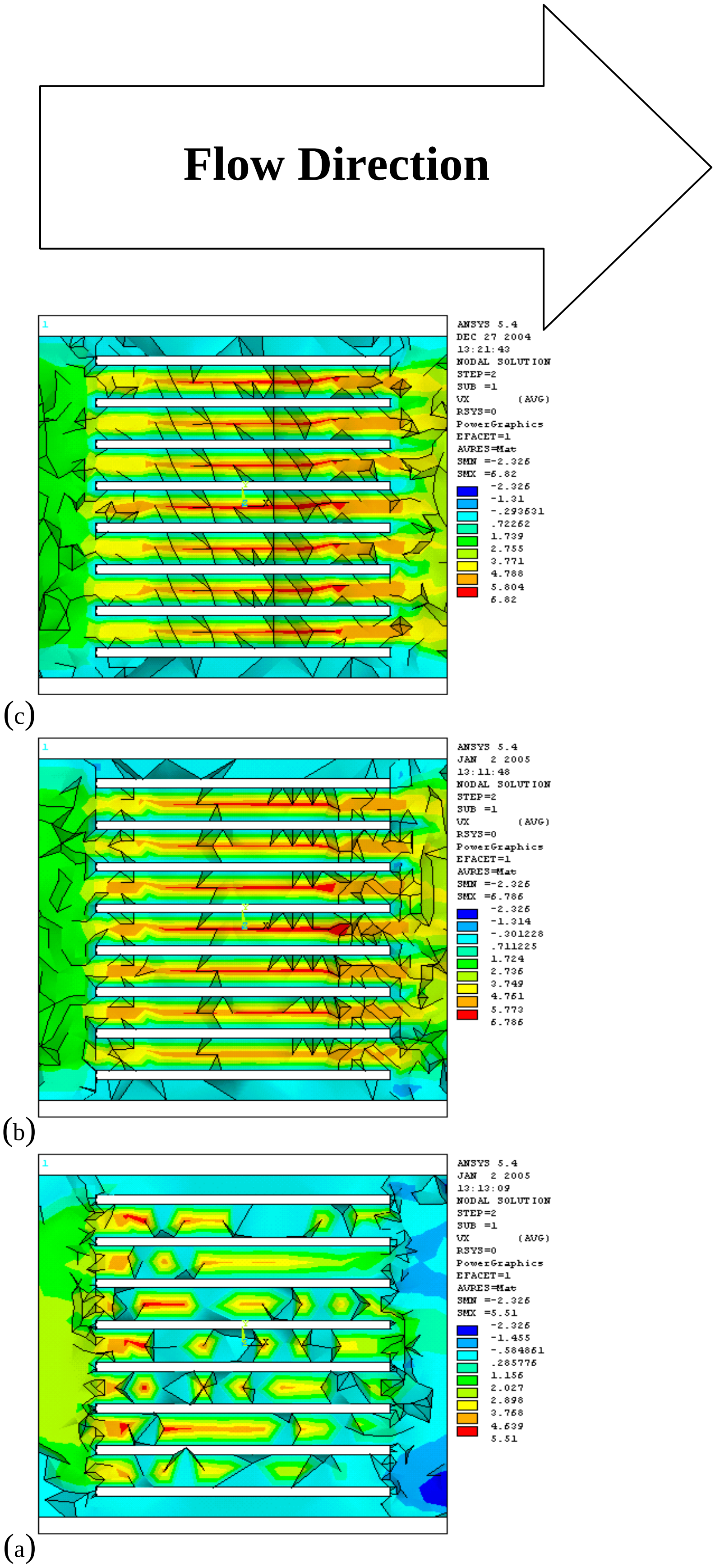

Fig. (19) Velocity Contour Map for Longitudinal Fins in the First Domain (a), Second domain (b), Third Domain (c) (Numerical).